First-principles studies of lone-pair-induced distortions in epitaxial phases of perovskite SnTiO_{3} and PbTiO_{3}

Krishna Chaitanya Pitike, William D. Parker, Lydie Louis, and Serge M. Nakhmanson

Phys. Rev. B **91**, 035112 — Published 12 January 2015

DOI: 10.1103/PhysRevB.91.035112

First-principles studies of lone-pair-induced distortions in epitaxial phases of perovskite $SnTiO_3$ and $PbTiO_3$

Krishna Chaitanya Pitike,[1] William D. Parker,[2,3] Lydie Louis,[1] and Serge M. Nakhmanson[1,*]

[1]*Department of Materials Science & Engineering, and Institute of Materials Science, University of Connecticut, Storrs, Connecticut 06269, USA*

[2]*Argonne Leadership Computing Facility, Argonne National Laboratory, Argonne, Illinois 60439, USA*

[3]*School of Chemical Engineering, Purdue University, West Lafayette, Indiana 47907, USA*

(Dated: December 12, 2014)

In this project, a computational investigation utilizing density functional theory methods is carried out to elucidate the differences in stereochemical lone-pair activity of Pb^{2+} and Sn^{2+} A-site ions in epitaxial polar $ATiO_3$ perovskites. The contrasting tendencies for the lead- and tin-based compounds to form different phases — $Amm2$ for the former *vs* Cm for the latter — under biaxial tension are connected to the amount of charge concentrated within the lone pair lobes. Specifically, phases are energetically more preferable when as much charge as possible is dissipated out of the lobe, thus lowering the cost of Coulomb repulsions between the lone pair and the surrounding oxygen cage. Although a strong band gap tuning was predicted in (fictitious) $SnTiO_3$ during the tensile $P4mm \rightarrow Cm$ phase transformation [see Phys. Rev. B **84**, 245126 (2011)], we find the same effect to be considerably weaker in $PbTiO_3$. The insights gained about the electronic-level underpinnings of transitional behavior in such lone-pair active epitaxial ferroelectrics may be used in the design of a new generation of more efficient electromechanical and electrooptical devices.

PACS numbers: 77.84.-s,77.80.bn,77.55.fp,73.90.+f

I. INTRODUCTION

It is remarkable that a single family of $PbTiO_3$ based perovskite materials, such as lead zirconate titanate $PbZr_{1-x}Ti_xO_3$ (PZT)[1–4] and a variety of lead-based relaxor ferroelectrics,[1,5,6] is dominating the field of ferroelectric (FE) and piezoelectric applications. Outstanding polar, piezoelectric and dielectric properties of all of these compounds emanate from strong lattice distortions — specifically, large displacements of both Pb^{2+} and Ti^{4+} ions away from their centrosymmetric positions in the undistorted perovskite structure. On the level of underlying electronic phenomena, the nature of these distortions for both cations is attributed to cooperative pseudo Jahn-Teller effect (coop-PJTE).[7,8] Noncentrosymmetric distortion of the TiO_6 cluster is a typical PJTE case (usually identified in the literature as a "d^0"), when mixing of empty Ti($3d$) states with filled O($2p$) states results in a host of electronic configurations, whose near degeneracy is removed by a spontaneous displacement of Ti from the centroid of the O_6 octahedron. The presence of Pb^{2+} cations, carrying nonbonded $6s^2$ electrons, the so-called electron lone pair, establishes yet another PJTE distortive network, which induces large elastic deformations and electric polarization.

The need to avoid the inclusion of a toxic element, such as lead, into next-generation electroactive compounds stimulated a search for novel Pb-free materials possessing property responses of comparable (or greater) magnitudes.[9–14] However, developing suitable replacements remains a great challenge, as, paraphrasing the authors of Ref. 12, when performance, cost, ease of preparation and precursors availability are taken into account, PZT still remains the almost perfect all-around piezoelectric material. The exceptional piezoelectric properties of PZT, compared to only moderate piezoelectricity of $PbTiO_3$, are attributed to the emergence of a morphotropic phase boundary (MPB)[3,15–18] near the Zr:Ti = 52:48 and high mobility of FE domain walls, indicating that the existence of large PJTE-induced structural distortions is a necessary but not sufficient ingredient for attaining colossal property responses.

Naively, one can expect that tin (Sn), an isoelectronic "younger brother" of lead, would be its natural replacement. Unlike lead, tin is environmentally benign, being widely used for tableware in the form of pewter alloys since the beginning of the Bronze Age.[19] Tin is readily available in its 4+ oxidation state, e.g., in the form of Sn(IV) oxide, or SnO_2 (rutile, mineral cassiterite). In contrast, its 2+ oxidation state — the one whose behavior is also governed by strong ($5s^2$) electron lone-pair activity[20–23] and is highly desirable for technological applications — is much more elusive. For example, Sn(II) oxide, or SnO (litharge), is metastable with respect to transformation into SnO_2 at a wide range of oxygen pressures. Although a number of recent computational studies have suggested that substituting A = Sn^{2+} for Pb^{2+} in a polar perovskite (tetragonal $P4mm$) $ATiO_3$ structure results in piezo- and ferroelectric properties similar to, or exceeding those of bulk $PbTiO_3$,[24–26] conventional solid-state growth of this phase remains a daunting task. A conventional ceramic synthetic route requires high temperatures, which leads to facile Sn^{2+} disproportionation into Sn^{4+} and Sn metal,[26,27] and, as of this writing, there have been no reports of bulk perovskite $SnTiO_3$ being produced.

The apparent difficulties of this growth approach have not discouraged other attempts to harness the attractive chemical properties of the Sn^{2+} oxidation state. For example, doping (Ba,Ca)TiO_3 FE ceramics and the incipient FE $SrTiO_3$ with tin resulted in the enhancement[28–31] and emergence[32] of polar properties in both cases, attributed to the presence of Sn^{2+} ions in the perovskite A-site positions. A divalent tin-containing compound Sn_2TiO_4 (isostructural with the low temperature form of Pb_3O_4)[32–34] and a series of tungsten-

based compounds $SnWO_4$,[35,36] Sn_2WO_5 and Sn_3WO_6[37] have also been manufactured and characterized. However, none of these structures exhibit spectacular electroactive properties.

Modern epitaxial engineering techniques can stabilize metastable structures through artificial elastic boundary conditions (misfit strain) and/or rate-limited kinetics.[38] Therefore, they offer an alternative approach to avoid the restrictions imposed by bulk thermodynamics in order to grow novel materials with enhanced properties that have the potential to replace PZT in a variety of technological applications. A recent attempt to synthesize $SnTiO_3$ films on sapphire and perovskite substrates from ceramic SnO_2 and TiO_2 targets utilizing PLD produced nonpolar ilmenite-type structures with only traces of a second phase compatible with perovskite geometry.[39] An emergence of a centrosymmetric crystal structure indicates the loss of electron lone pair activity (along with the associated polar lattice distortions), suggesting that the Sn^{2+} oxidation state was not sufficiently achieved in the PLD-grown films.

In a previous computational study,[40] we have evaluated structural stability of tin titanate polymorphs with $SnTiO_3$ stoichiometry, focusing in particular on resolving phase transformations in the proposed epitaxial polar-perovskite phase. Our investigation showed that polymorphs possessing corner-sharing TiO_6 octahedra and polar cation displacements have lower energies, compared to centrosymmetric polymorphs, such as ilmenite-type structure. We also demonstrated that, although the stress-free ground state of polar-perovskite $SnTiO_3$ is the same as that of $PbTiO_3$ [i.e., tetragonal, with space group $P4mm$ and spontaneous polarization $\mathbf{P} \sim (0,0,c)$], under biaxial tension, the former compound undergoes a transition into a monoclinic Cm phase, $\mathbf{P} \sim (a,a,c)$, while the latter transitions to the $Amm2$ phase, $\mathbf{P} \sim (a,a,0)$.[41,42] All of the aforementioned structures, together with the nonpolar cubic $Pm\bar{3}m$ aristotype, are depicted in Fig. 1. The drastic reduction of symmetry caused by the $P4mm \rightarrow Cm$ phase transformation induces a large change in the value of the $SnTiO_3$ electronic band gap $E_{\rm gap}$, which could potentially be tuned elastically, by flexing the substrate, or electrically, by applying an electric field.

Although we were able to resolve the electronic-level underpinnings of the dramatic $E_{\rm gap}$ variation in epitaxial perovskite $SnTiO_3$ (see Section VI and Fig. 5 in Ref. 40), it remained unclear why its transitional behavior under biaxial tension is different from that of $PbTiO_3$. Furthermore, with the proposed $E_{\rm gap}$ opening mechanism being quite generic, it was interesting to investigate how pronounced the same effect would be in epitaxial $PbTiO_3$ as it undergoes a transition into the more symmetric $Amm2$ phase.

In this study, we utilize first-principles density-functional-theory(DFT)-based calculations to address both of these questions. We find that the $E_{\rm gap}$ tuning effect in $P4mm \rightarrow Amm2$ $PbTiO_3$ is much weaker than in $P4mm \rightarrow Cm$ $SnTiO_3$. We then trace the contrasting transitional behavior of $PbTiO_3$ and $SnTiO_3$ to differences in stereochemical lone-pair activity of Pb^{2+} and Sn^{2+} ions. Specifically, we demonstrate that optimization of repulsive Coulomb interactions between negatively charged oxygen ions — comprising the cuboctahedral cage around the A^{2+} cation — and the electron lone-pair charge cloud leads to dissimilar spatial orientations of the latter in the tin- and lead-based compounds.

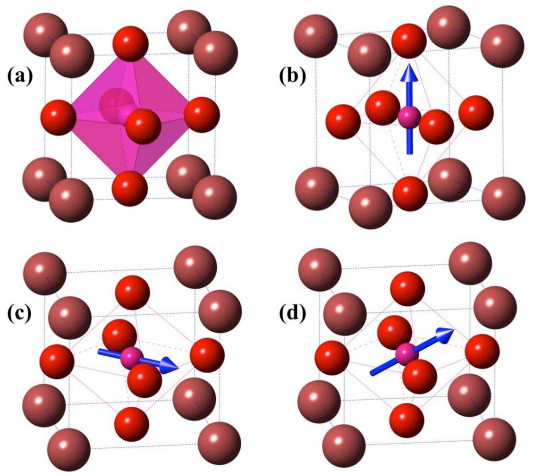

FIG. 1. (Color online) Crystal structure of **(a)** cubic perovskite $ATiO_3$ aristotype, space group $Pm\bar{3}m$, and its polar distortions leading to non-centrosymmetric structures with the following symmetries: **(b)** $P4mm$, $\mathbf{P} \sim (0,0,c)$, **(c)** $Amm2$, $\mathbf{P} \sim (a,a,0)$, and **(d)** Cm, $\mathbf{P} \sim (a,a,c)$. TiO_6 coordination cages are represented by semi- ($Pm\bar{3}m$) and completely (all other phases) translucent polyhedra while Sn atoms are shown in pink (dark gray). Arrows attached to the Ti ion indicate the direction of polarization in the non-centrosymmetric structures **(b–d)**.

II. COMPUTATIONAL DETAILS

All DFT calculations presented in this study were performed using the Vienna Ab initio Simulation Package (VASP)[43,44] and QUANTUM ESPRESSO[45] (QE) within the local density approximation (LDA), parameterized by Perdew and Zunger.[46] Projector-augmented plane-wave method[47,48] with 900 eV energy cutoff was utilized in VASP, with the following electronic configurations for the involved elements: Pb ($5d^{10}6s^26p^2$), Sn ($4d^{10}5s^25p^2$), Ti ($2p^63d^24s^2$) and O ($1s^22s^22p^4$). In calculations done with QE, electronic wave functions (density) were expanded in plane waves up to 30 Ry (300 Ry) and valence electrons were treated with Vanderbilt ultrasoft[49] pseudopotentials. Pseudovalence electronic configurations in the ultrasoft pseudopotentials were identical to those of the projector-augmented wave pseudopotentials for Pb and Sn but differed in Ti ($3s^23p^64s^23d^1$) and O ($2s^22p^4$).[50] Zone-edge-shifted $8 \times 8 \times 8$ Monkhorst-Pack (MP)[51] k-point meshes were used for the Brillouin zone (BZ) integrations with both simulation packages. Gaussian smearing value of 0.05 eV was used to produce the electronic density of states (EDOS) plots. In all calculations, internal ionic positions were relaxed to forces of less than 10^{-3} eV/Å. During unit-cell shape optimization, the appropriate stress-tensor components were converged to values of less than 0.1 kbar. Biaxial misfit strain in a thin film constrained on a cubic (001)-oriented substrate was simulated by varying the in-plane lattice constant a of the tetragonal unit cell and allowing the

out-of-plane lattice constant c to relax by converging the normal stress in the out-of-plane direction to a value of less than 0.1 kbar while keeping the imposed polar symmetry intact. No monoclinic distortions were allowed for the unit cell of the Cm structure by setting all shear stress-tensor components to zero. The biaxial misfit strain was defined as $\varepsilon = a/a_0 - 1$, where a_0 corresponds to the optimized lattice parameter of a structure with all the normal stresses relaxed to values less than 0.1 kbar. Adopting these settings resulted in essentially the same structural and electronic properties obtained with either simulation package for any of the considered $ATiO_3$ (A = Pb, Sn) polymorphs [mean absolute differences: in energy difference – 0.005 eV/f.u., in lattice parameter – 0.011 Å, in tetragonality – 0.002, and in Kohn-Sham band gap – 0.049 eV].

Electron localization functions (ELFs) are customarily used to visualize electron lone pairs: usually to highlight the pronounced differences between the electron cloud shapes of centrosymmetric non-polar and non-centrosymmetric polar phases or polymorphs of the same material.[36,52–54] However, when comparing the ELF plots of the *structurally similar* $P4mm$, $Amm2$ and Cm phases for the $ATiO_3$ perovskite structure — all non-centrosymmetric and polar, but with different directions of the unit-cell polarization vector — we did not observe any noticeable distinctions among them. Alternatively, following an approach of Watson and coworkers[20,22,23,55,56] that utilizes energy-resolved, or *partial,* electron charge density maps to visualize specific regions of the EDOS that are associated with the asymmetric nature of lone pairs allowed us to resolve the distinctions among these phases, as discussed in detail in section III B. Partial electron charge density maps presented in that section were created using the VESTA[57] software package.

III. RESULTS AND DISCUSSION

A. Structure and band gap tuning

In Table I, we collect relative energies, lattice parameters, and $E_{\rm gap}$ values for the representative polar phases, as well as for the non-polar cubic phase, of perovskite $SnTiO_3$ and $PbTiO_3$. All of these phases were relaxed to small normal stresses while keeping their symmetries intact under the condition that no shear distortions are allowed. For both compounds, polar tetragonal $P4mm$ structures are found as the lowest energy stress-free phases that occur under biaxial compression with respect to the optimized lattice constant of the cubic aristotype phase. Although experimental values of the lattice parameters are unavailable for the (as of now fictitious) perovskite $SnTiO_3$ structure, comparison of the computed values of a and c in the $P4mm$ phase of $PbTiO_3$ with experimental results [see, e.g., Ref. 58] shows that they are underestimated by 0.94% and 2.9%, respectively, which is typical accuracy for DFT-LDA. The computed LDA band gap of $PbTiO_3$ is severely (∼54%) underestimated[59] and we expect the same to be true for the $SnTiO_3$ structure. However, the trends in the relative valence-band maximum (VBM) and conduction-band minimum (CBM) changes with respect to varying epitaxial strain and polarization direction rotation — that are discussed in more detail below — should still be robust.

TABLE I. Energy differences (ΔE) per formula unit (f.u.) with respect to the lowest energy phase for all the considered perovskite $ATiO_3$ (A = Pb, Sn) structures. Here and in what follows, the phases are arranged in the order of decreasing symmetry. For both tin- and lead-based compounds, the $P4mm$ phase has the lowest energy, which is taken as zero. Lattice parameters and band gap values $E_{\rm gap}$ are also presented for all the structures. Values in parentheses (calculated using ultrasoft instead of PAW pseudopotentials) are shown to illustrate the comparability of results from the two methods on these systems.

	ΔE (eV/f.u.)	a (Å)	c/a	$E_{\rm gap}$ (eV)
		$SnTiO_3$		
$Pm\bar{3}m$	0.341 (0.325)	3.871 (3.861)	1.000	0.905 (0.927)
$P4mm$	0.000	3.786 (3.784)	1.134 (1.123)	0.694 (0.732)
$Amm2$	0.053 (0.049)	3.957 (3.945)	0.965 (0.965)	0.983 (1.034)
Cm	0.036 (0.033)	3.913 (3.901)	0.999 (1.000)	1.402 (1.448)
		$PbTiO_3$		
$Pm\bar{3}m$	0.059 (0.057)	3.890 (3.879)	1.000	1.471 (1.562)
$P4mm$	0.000	3.865 (3.852)	1.044 (1.044)	1.489 (1.535)
$Amm2$	0.013 (0.012)	3.930 (3.917)	0.984 (0.985)	1.778 (1.710)
Cm	0.015 (0.014)	3.907 (3.895)	1.000 (1.000)	1.895 (1.927)

The magnitudes of polar cation distortions in all of the aforementioned $ATiO_3$ (A = Pb, Sn) hettotypes are assembled in Table II. The displacements of Sn^{2+} ion away from the center of the surrounding cuboctahedral oxygen cage are almost twice as large as those of the Pb^{2+} ion. Furthermore, Ti^{4+} off-centerings inside their octahedral oxygen cages in $SnTiO_3$, are also, on average 50–60% more pronounced than those in $PbTiO_3$. This increased off-centering is remarkable considering that the unit-cell volumes of both compounds are quite similar (mean absolute difference of 0.6 $Å^3$/f.u. between isomorphs). Combination of both cation distortions results in a much stronger polarization in $SnTiO_3$ (∼1.2 C/m^2; see Ref. 40 for details) as compared to its lead-based counterpart.

TABLE II. Polar off-centerings (Å) of A and Ti ions in the considered perovskite $ATiO_3$ (A = Pb, Sn) structures. These displacements are computed with respect to the center of mass of the oxygen cage surrounding the appropriate cation: 12-atom cuboctahedral cage for Pb and Sn, and 6-atom octahedral cage for Ti.

	$P4mm$			$Amm2$			Cm		
	x	y	z	x	y	z	x	y	z
				$SnTiO_3$					
Sn	0.000	0.000	0.737	0.407	0.407	0.000	0.345	0.345	0.340
Ti	0.000	0.000	0.470	0.231	0.231	0.000	0.181	0.181	0.177
				$PbTiO_3$					
Pb	0.000	0.000	0.395	0.229	0.229	0.000	0.178	0.178	0.180
Ti	0.000	0.000	0.261	0.152	0.152	0.000	0.118	0.118	0.119

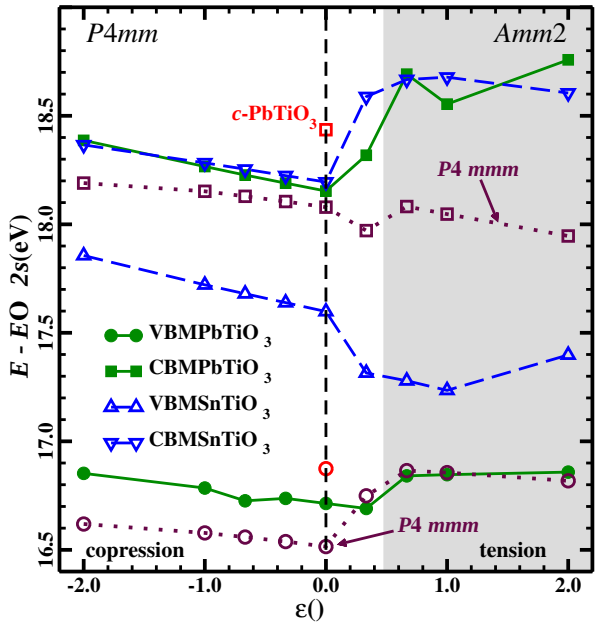

FIG. 2. (Color online) VBM [circles] and CBM [squares] of epitaxially strained $PbTiO_3$ across the $P4mm \rightarrow Amm2$ phase transition as functions of biaxial strain. The same data for the $P4/mmm$ $PbTiO_3$ structure is shown in dotted lines. Open (red) square and circle at zero strain mark the VBM and CBM positions in the cubic $Pm\bar{3}m$ structure. VBM and CBM data for the $P4mm \rightarrow Cm$ phase transformation in $SnTiO_3$ [same as in Fig. 4 of Ref. 40] is also presented here in dashed lines. The CBM/VBM curves for $SnTiO_3$ are shifted to match the CBM values of both compounds in the $P4mm$ phase.

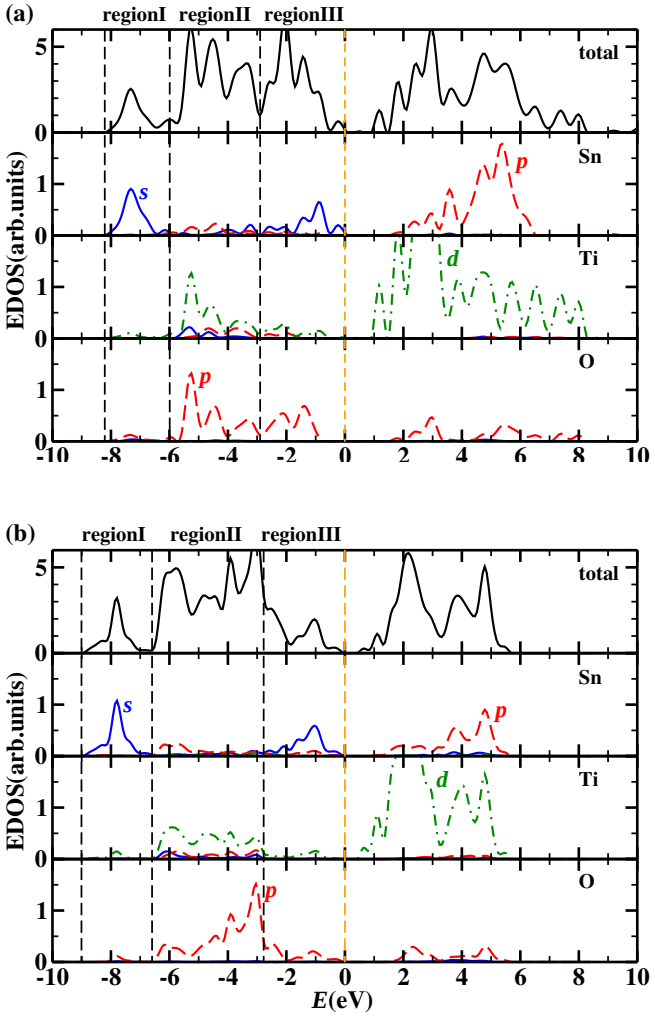

FIG. 3. (Color online) Total and partial, i.e., ion and l quantum number resolved, EDOS for **(a)** $Pm\bar{3}m$ non-polar cubic and **(b)** $P4mm$ polar tetragonal phases of perovskite $SnTiO_3$ showing three energy regions utilized for visualization of partial electron charge density maps. These regions are identified individually for each phase.

Turning to the transitional behavior of the $ATiO_3$ compounds, under biaxial tension, the lowest-energy $P4mm$ phase for both A = Pb and Sn initially transforms into the Cm structure. However, the epitaxial stability interval of the latter is very narrow in $PbTiO_3$, and the polarization vector quickly rotates into the xy-plane as tension is further increased, resulting in a state with $Amm2$ symmetry [data not shown]. The observed $P4mm \rightarrow Amm2$ phase transition in $PbTiO_3$ is in agreement with previous computational results obtained with comparable DFT-based approaches.[41,42] At variance, in $SnTiO_3$, the Cm state persists for a wide range of tensile strains with no traces of $Amm2$ phase observed even for relatively large biaxial tensions.[40] It is noteworthy that both of the representative (stress-free) tensile phases in $PbTiO_3$ have rather similar structural parameters and are close to each other in energy, the $Amm2$ state being only 2 meV lower than the Cm one, while, in $SnTiO_3$ we see much stronger variations in the relative energies (∼20 meV) and structural parameters of the involved polar phases.

As shown in Table I for the representative polar phases and in Fig. 2 for the complete ±2% interval of epitaxial strains, the E_{gap} tuning during the $P4mm \rightarrow Amm2$ phase transition in $PbTiO_3$ is limited to 0.2–0.3 eV (slightly more if the borderline Cm phase could be stabilized). Therefore, although the generic trend for the band gap opening under lowering structural symmetry is indeed present in $PbTiO_3$, individual differences between the DFT-based E_{gap} values of various phases are small. This is in sharp contrast with the large effect (∼0.7 eV or 100% change) observed for the $P4mm \rightarrow Cm$ phase transition in $SnTiO_3$, according to the Table I data for the representative phases and the ±2% epitaxial strain interval dependencies shown in Fig. 4 of Ref. 40 and repeated here in Fig. 2. In general, we obtain much smaller E_{gap} values in $SnTiO_3$ than in $PbTiO_3$. This band gap reduction could be attributed to the stronger interaction between the Sn($5s$) and O($2p$) orbitals compared to that of Pb($6s$) and O($2p$), which leads to a more pronounced upward shift of the antibonding s-p hybrids that constitute the top of the valence band.[36] It is also noteworthy that the weakness of the A(s)–O(p) interactions in $PbTiO_3$, as well as their relative insensitivity to the direction of the polar structural distortion, results in the flatness of the VBM level inside this ±2% epitaxial strain interval (see filled-circle curve in Fig. 2).

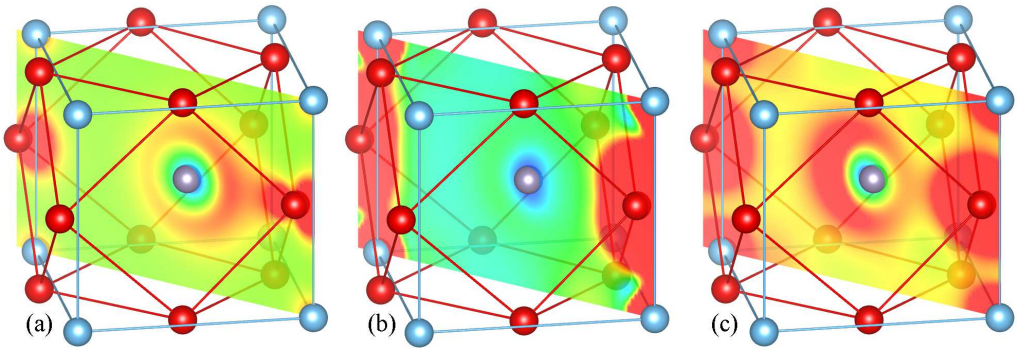

FIG. 4. (Color online) Partial charge density maps in energy regions **(a)** I, **(b)** II, and **(c)** III in the (110) plane of the $Amm2$ phase of $SnTiO_3$. Here, unlike the Ti-centered units of Fig. 1, cells are centered on the A^{2+} cation with its cuboctahedral coordination cage explicitly outlined in red. Sn, Ti, and O ions are represented by gray, light blue (light gray), and red (dark gray) spheres, respectively. Contour levels shown are between 0 (blue) and 0.16 e/Å^3 (red).

B. Electronic density of states and lone pair activity

Fig. 3 presents total and partial (ion- and l quantum number-resolved) EDOS in **(a)** $Pm\bar{3}m$ non-polar cubic and **(b)** $P4mm$ polar tetragonal phases of perovskite $SnTiO_3$. For each phase, following the approach of Watson and coworkers,[20,22,23,55,56] valence bands are divided into three regions that highlight specific interactions among the pseudoatomic wave functions centered on various ions. The same information was also obtained for all other structures considered in this investigation [data not shown]. Only minor differences were found in the shapes of the EDOS curves for all the polar variants of each $ATiO_3$ (A = Sn, Pb) compound.

For each phase of $SnTiO_3$ and $PbTiO_3$, the respective values of partial densities of the A^{2+} ion s and p states, as well as the oxygen $2p$ states, define the boundaries between the regions. Region I, lying approximately between -9 and -6 eV, encompasses the highly pronounced EDOS peak for the A(s) states and highlights bonding interactions between them and O($2p$), with a small admixture of Ti($3d$). The boundary between regions I and II is placed at the minimum that separates the A(s) EDOS states peak from the neighboring peak at higher energy. Region II, extending from that boundary to approximately -3, or -3.5 eV, is comprised mostly of EDOS parts that correspond to bonding interactions between Ti($3d$) and O($2p$) states with some contributions from A(p). The boundary between regions II and III is assigned to the energy where the A(s) states density again becomes denser than that of the A(p) states, as another A(s) EDOS peak is formed within region III. Region III, spanning from this boundary to the Fermi level, is formed by EDOS parts that include antibonding interactions of A(s) and O($2p$) states, also with a small admixture of A(p). Region boundaries are determined individually for each particular material/phase combination. Small variations in their location do not appreciably change the results of our calculations. For example, boundary assignments for the non-polar $Pm\bar{3}m$ and $P4mm$ polar tetragonal phases of perovskite $SnTiO_3$ are shown in Fig. 3.

In Fig. 4, we present partial charge density maps corresponding to energy regions I, II and III using the $Amm2$ phase of $SnTiO_3$ as an example. The aforementioned specific interactions — bonding between Sn and O in region I, bonding between Ti and O in region II, and antibonding between Sn and O in region III — are visualized in panels **(a)**, **(b)** and **(c)**, respectively. The classical picture of orbital hybridization, where an electron lone pair is formed as a result of intra-atomic mixing of s and p orbitals on the same cation,[60,61] places the associated charge density into region I. This hybrid orbital is chemically inert, but sterically active, and is projected to the side of the cation, distorting the lattice. That is clearly not the case for the partial charge density in region I, shown in Fig. 4**(a)** –the density is rather round in shape and thus does not have the required directionality that would promote steric activity [this same behavior in region I was obtained for all the other structures considered here]. Only relatively recent computational investigations for a variety of materials have proven that lone-pair electronic states are more subtle than the classical picture suggests: the interactions between the cation s and p orbitals are actually mediated through the p orbitals of the neighboring anion.[20–23,53,54] This interaction mechanism can be interpreted as a double PJTE where the anion p states insert themselves in the middle of the energy gap between the cation states and then hybridize with the s states below, and p states above. Therefore, currently, the lone pair is identified as a complex cation(s,p)–anion(p) hybrid formed by combinations of electron bands that are positioned right below the Fermi level. These bands correspond to the partial charge density residing in energy region III. Our results for $SnTiO_3$ agree with the previous findings[20–23,53,54] showing the characteristic asymmetric charge density lobe within region III situated to the side of the cation and pointing away from the nearest oxygen, as depicted in Fig. 4**(c)**.

In Fig. 5, we present 'region III' partial charge density maps for the polar $P4mm$, $Amm2$ and Cm phases, as well as for the non-polar $Pm\bar{3}m$ phase in both $SnTiO_3$ and $PbTiO_3$. Just as described in the previous paragraph, in all polar phases, we observe asymmetric charge density distributions associated with stereochemical electron lone pair activity while, in non-polar $Pm\bar{3}m$ phases, such charge density distributions have spherical symmetry. Using the same arguments as in the investigation of tungsten-based AWO_4 (A = Sn, Pb) compounds,[36] we interpret these visualization results as the Sn^{2+} lone pairs being "more compact" and the Pb^{2+} ones "more diffuse."

To evaluate the amount of electron charge Q contained

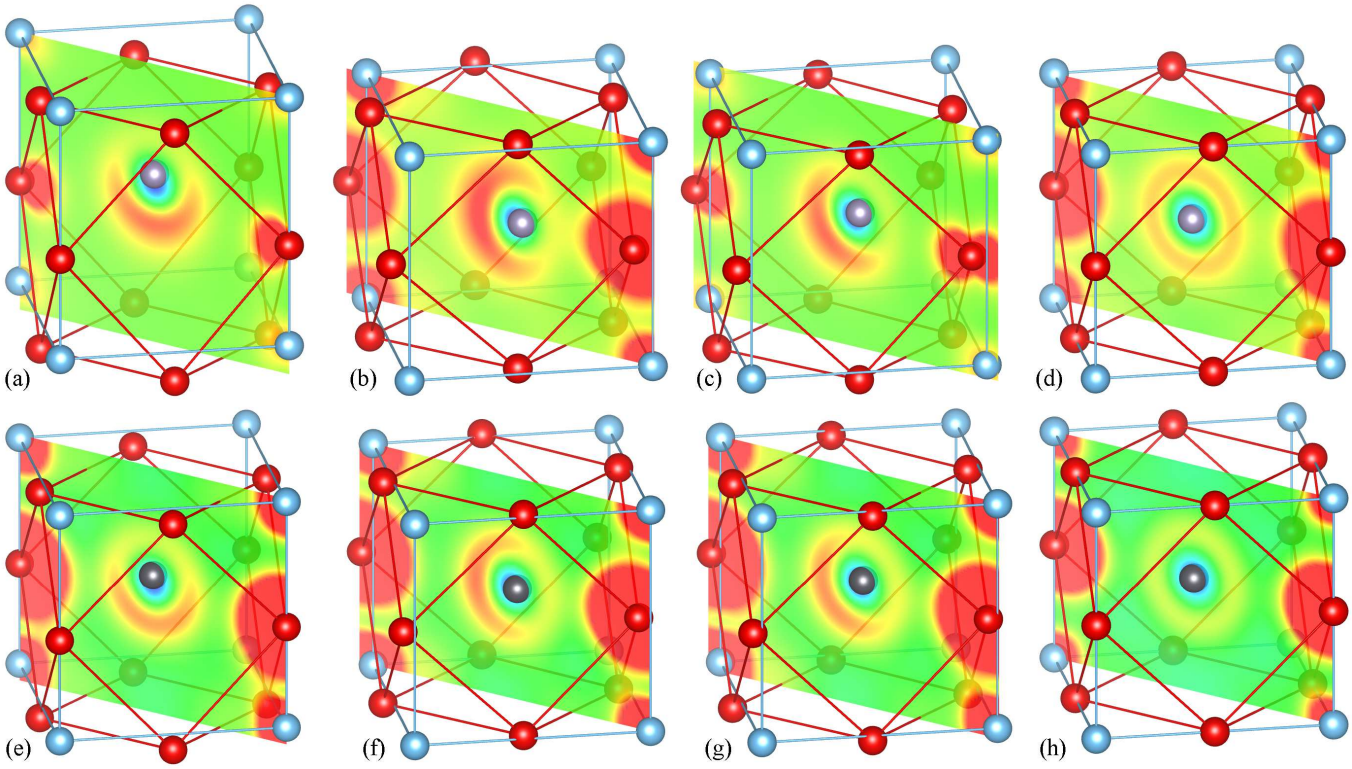

FIG. 5. (Color online) Region III partial charge density maps in the (110) plane, depicting the characteristic asymmetric charge-density lobes associated with stereochemically active electron lone pairs in $ATiO_3$ (A = Pb, Sn). Just as in Fig. 4, A^{2+} cation-centered cells are used, with A^{2+}, Ti, and O ions represented by gray, light blue (light gray) and red (dark gray) spheres, respectively. $SnTiO_3$ structures are shown in the top row: **(a)** $P4mm$, **(b)** $Amm2$, **(c)** Cm, and **(d)** non-polar $Pm\bar{3}m$. $PbTiO_3$ structures are assembled in the bottom row: **(e)** $P4mm$, **(f)** $Amm2$, **(g)** Cm and **(h)** non-polar $Pm\bar{3}m$. Contour levels shown are between 0 (blue) and 0.24 (red) for $SnTiO_3$, and 0 (blue) and 0.16 e/Å^3 (red) for $PbTiO_3$.

within the lone pair lobe (or sphere, in the case of non-polar geometries) in each structure, we numerically integrated the 'region III' partial charge density inside a volume V around the A-site ion, including all the grid points with charge density that are greater than some small value S. The shape of the volume V, as well as the smallness of charge-density iso-surface cutoff S, and the position of the boundary separating energy regions II and III, were varied to verify that the resulting lone-pair charges do not change appreciably. The values of V, Q, and S are assembled in Table III. Two major differences in the properties of Sn^{2+} and Pb^{2+} lone pairs stand out: first, although all the integrated charges are considerably smaller than the formal charge of $2e$, for the structures of the same symmetry, charge found for the Sn^{2+} lone pair is, on average, twice as large as that found for the Pb^{2+} lone pair; and second, volumes surrounding the lone-pair charges in $SnTiO_3$ structures are also larger than those in their lead-based counterparts. Therefore, refining the argument presented in the previous paragraph, we can claim that, in perovskite $ATiO_3$ structures, A = Sn^{2+} lone pairs *carry slightly more charge* per unit volume than those of A = Pb^{2+}. However, it would be incorrect to regard the former ones as "more compact" since they occupy more space.

TABLE III. Total charge Q integrated around the A = Pb, Sn ion within the volume V enclosed by the iso-surface with charge density S, calculated for all the considered perovskite $ATiO_3$ phases. Average lone-pair charge densities Q/V are shown in the last column.

	S (e/Å^3)	V (Å^3)	Q (e)	Q/V (e/Å^3)
		$SnTiO_3$		
$Pm\bar{3}m$	0.0154	4.076	0.473	0.116
$P4mm$	0.0090	5.348	0.580	0.108
$Amm2$	0.0126	5.550	0.741	0.134
Cm	0.0090	5.292	0.567	0.107
		$PbTiO_3$		
$Pm\bar{3}m$	0.0086	3.543	0.250	0.071
$P4mm$	0.0106	3.697	0.350	0.095
$Amm2$	0.0114	3.374	0.328	0.097
Cm	0.0114	2.591	0.339	0.131

Furthermore, we can infer a yet more subtle observation connected to the transitional behavior of both compounds under epitaxial tension from the results of Table III. For $SnTiO_3$, comparing the lone pair charges of the tensile polar phases, we see that $Q(Cm)$ is substantially smaller (by $\sim 0.17e$) than $Q(Amm2)$. On the other hand, for $PbTiO_3$, $Q(Cm)$ is slightly larger (by $\sim 0.01e$) than $Q(Amm2)$. Thus, we can conclude that, in each case, the system prefers to tran-

sition into a phase that possesses a smaller lone-pair charge, specifically, the Cm phase for $SnTiO_3$ and $Amm2$ phase for $PbTiO_3$. The same trend can also be seen for the polar structure lone-pair charge densities Q/V: they are, on average, 20% higher in the metastable phases ($Amm2$ for $SnTiO_3$ and Cm for $PbTiO_3$), compared to those that actually occur during the phase transition. For each compound, the magnitude of the charge difference between the competing phases tracks the size of their energy difference ΔE, shown in Table I. So, the stronger energetic preference of $SnTiO_3$ to adopt the Cm symmetry in tension is connected to a significant draining effect that this geometrical conformation has on the lone pair charge Q. Conversely, for $PbTiO_3$, the lone pair charges of both phases are very close, which results in a rather weak anisotropy of polar distortions. We have already shown before that, under certain conditions, Pb^{2+} ions can exhibit similar behavior, which may lead to almost complete loss of directional anisotropy of their polar off-centerings.[62]

Finally, we point out that, for both compounds, the stable $P4mm$ phase is exempt from the "minimal Q" rule, having a lone-pair charge that is 0.01–0.02e *higher* than that of the preferred tensile phase. This exemption may be explained when, in addition to the lone pair activity, we consider distortions inside the TiO_6 unit, where Ti displacements along the [001] direction, i.e., toward a corner of the octahedron, are always heavily favored[63] (note that Ti and Pb off-centerings happen in lockstep). Therefore, minimization of the repulsive Coulomb interactions between the A-site cation lone pair and the negatively charged oxygen cage surrounding it becomes more important only when Ti is forced to off-center along a sub-optimal direction, such as toward an edge ($Amm2$) or a face (Cm) of the octahedral unit.

IV. CONCLUSIONS

In this project, following the results of our previous DFT-based study of epitaxial phases of a fictitious perovskite ferroelectric $SnTiO_3$ and, specifically, the prediction of a large band gap tuning during the polarization-rotation phase transition under biaxial tension,[40] we have investigated the same effect in epitaxial $PbTiO_3$, a well-known ferroelectric material that is isoelectronic to $SnTiO_3$. We found the band gap tuning in $PbTiO_3$ to be considerably weaker than in $SnTiO_3$. This relatively weaker tunability may be attributed to **(i)** higher symmetry of the preferred $Amm2$ tensile phase in the lead-based compound compared to Cm in $SnTiO_3$, and **(ii)** weaker interactions of Pb($6s$) and O($2p$) orbitals that do not exhibit a pronounced dependence on the direction of the polar distortion. This lack of dependence on polar distortion results in a flatness of the $PbTiO_3$ VBM level across the $P4mm \rightarrow Amm2$ phase transition.

We then investigated the stereochemical lone-pair activity of Pb^{2+} and Sn^{2+} ions in polar-perovskite $ATiO_3$ hettotypes possessing $P4mm$, $Amm2$, and Cm symmetries. Structural differences among these phases stem from distinct spatial orientations of the lone-pair charge cloud within the cuboctahedral oxygen cage around the A^{2+} cation. The contrasting tendencies for $PbTiO_3$ and $SnTiO_3$ to form different phases under epitaxial tension were linked to the amount of charge concentrated within the lone pair lobes. Specifically, in the energetically more stable tensile phase, as much charge as possible is transferred out of the lobe, which lowers the cost of Coulomb repulsion between the lone pair and the surrounding negatively charged oxygen cage.

These insights into the electronic-level underpinnings of transitional behavior and functional property tuning in epitaxial ferroelectrics, such as $PbTiO_3$ and $SnTiO_3$, will be useful for the design of a new generation of more efficient electromechanical and electrooptical devices.

ACKNOWLEDGMENTS

The authors are thankful to the National Science Foundation (DMR 1309114) for funding this project. SMN acknowledges Peter Zapol and Christos Takoudis for many useful discussions.

* smn@ims.uconn.edu

[1] K. Uchino, *Ferroelectric devices*, Vol. 16 (CRC Press, 2000).
[2] B. Jaffe, W. R. Cook, and H. Jaffe, *Piezoelectric ceramics* (Academic Press, 1971).
[3] M. Ahart, R. E. Cohen, P. Ganesh, P. Dera, H.-K. Mao, R. J. Hernley, Y. Ren, P. Liermann, and Z. Wu, Nature **451**, 545 (2008).
[4] H. N. Lee, S. M. Nakhmanson, M. F. Chisholm, H. M. Christen, K. M. Rabe, and D. Vanderbilt, Phys. Rev. Lett. **98**, 217602 (2007).
[5] S.-E. Park and T. R. Shrout, J. Appl. Phys. **82**, 1804 (1997).
[6] Z. Kutnjak, J. Petzelt, and R. Blinc, Nature **441**, 956 (2006).
[7] I. B. Bersuker, Ferroelectrics **164**, 75 (1995).
[8] I. B. Bersuker, *The Jahn-Teller Effect* (Cambridge University Press, 2006).
[9] Y. Saito, H. Takao, T. Tani, T. Nonoyama, K. Takatori, T. Homma, T. Nagaya, and M. Nakamura, Nature **432**, 84 (2004).
[10] T. R. Shrout and S. J. Zhang, J. Electroceram. **19**, 113 (2007).
[11] J. Rodel, W. Jo, K. T. P. Seifert, E.-M. Anton, T. Granzow, and D. Damjanovic, J. Am. Ceram. Soc. **92**, 1153 (2009).
[12] D. Damjanovic, N. Klein, J. Li, and V. Porokhonskyy, Functional Mater. Lett. **03**, 5 (2010).
[13] J. W. Bennett, I. Grinberg, P. K. Davies, and A. M. Rappe, Phys. Rev. B **83**, 144112 (2011).
[14] R. Armiento, B. Kozinsky, M. Fornari, and G. Ceder, Phys. Rev. B **84**, 014103 (2011).
[15] H. Fu and R. E. Cohen, Nature **403**, 281 (2000).
[16] R. Guo, L. E. Cross, S.-E. Park, B. Noheda, D. E. Cox, and G. Shirane, Phys. Rev. Lett. **84**, 5423 (2000).
[17] B. Noheda, Curr. Opin. Solid State Mater. Sci. **6**, 27 (2002).
[18] Z. Wu and R. E. Cohen, Phys. Rev. Lett. **95**, 037601 (2005).
[19] C. Hull, *Pewter* (Shire Publications Ltd, 2005).
[20] G. W. Watson and S. C. Parker, J. Phys. Chem. B **103**, 1258 (1999).
[21] G. W. Watson, S. C. Parker, and G. Kresse, Phys. Rev. B **59**, 8481

(1999).
[22] G. W. Watson, J. Chem. Phys. **114**, 758 (2001).
[23] A. Walsh and G. W. Watson, Phys. Rev. B **70**, 235114 (2004).
[24] Y. Konishi, M. Ohsawa, Y. Yonezawa, Y. Tanimura, T. Chikyow, H. Koinuma, A. Miyamoto, M. Kubo, and K. Sasata, Mat. Res. Soc. Symp. Proc. **748**, U3.13.1 (2003).
[25] Y. Uratani, T. Shishidou, and T. Oguchi, Jpn. J. Appl. Phys. **47**, 7735 (2008).
[26] S. Matar, I. Baraille, and M. Subramanian, Chem. Phys. **355**, 43 (2009).
[27] M. S. Moreno, G. Punte, G. Rigotti, R. C. Mercader, A. D. Weisz, and M. A. Blesa, Solid State Ionics **144**, 81 (2001).
[28] S. Suzuki, T. Takeda, A. Ando, and H. Takagi, App. Phys. Lett. **96**, 132903 (2010).
[29] S. Suzuki, T. Takeda, A. Ando, T. Oyama, N. Wada, H. Niimi, and H. Takagi, Jpn. J. Appl. Phys. **49**, 09MC04 (2010).
[30] S. Suzuki, A. Honda, S. Higai, A. Ando, N. Wada, and H. Takagi, Jpn. J. Appl. Phys. **50**, 09NC11 (2011).
[31] S. Suzuki, A. Honda, N. Iwaji, S. Higai, A. Ando, H. Takagi, H. Kasatani, and K. Deguchi, Phys. Rev. B **86**, 060102 (2012).
[32] N. Kumada, Y. Yonesaki, T. Takei, N. Kinomura, and S. Wada, Mater. Res. Bull. **44**, 1298 (2009).
[33] E. J. Baran, A. C. González-Baró, N. Kumada, N. Kinomura, T. Takei, and Y. Yonesaki, J. Alloys Comp. **490**, L12 (2010).
[34] S. Ohara, H. Takizawa, and Y. Hayashi, Chem. Lett. **39**, 364 (2010).
[35] W. Jeitschko and A. W. Sleight, Acta Crystallogr. Sect. B **28**, 3174 (1972).
[36] M. W. Stoltzfus, P. M. Woodward, R. Seshadri, J.-H. Klepeis, and B. Bursten, Inorg. Chem. **46**, 3839 (2007).
[37] H. Y. Chang, K. M. Ok, J. H. Kim, P. S. Halasyamani, M. Stoltzfus, and P. Woodward, Inorg. Chem. **46**, 7005 (2007).
[38] P. A. Salvador, T.-D. Doan, B. Mercey, and B. Raveau, Chem. Mater. **10**, 2592 (1998).
[39] T. Fix, S.-L. Sahonta, V. Garcia, J. L. MacManus-Driscoll, and M. G. Blamire, Cryst. Growth Des. **11**, 1422 (2011).
[40] W. D. Parker, J. M. Rondinelli, and S. M. Nakhmanson, Phys. Rev. B **84**, 245126 (2011).
[41] C. Bungaro and K. M. Rabe, Phys. Rev. B **69**, 184101 (2004).
[42] O. Diéguez, K. M. Rabe, and D. Vanderbilt, Phys. Rev. B **72**, 144101 (2005).
[43] G. Kresse and J. Furthmüller, Comput. Mater. Sci. **6**, 15 (1996).
[44] G. Kresse and J. Furthmüller, Phys. Rev. B **54**, 11169 (1996).
[45] P. Giannozzi, S. Baroni, N. Bonini, M. Calandra, R. Car, C. Cavazzoni, D. Ceresoli, G. L. Chiarotti, M. Cococcioni, I. Dabo, A. D. Corso, S. de Gironcoli, S. Fabris, G. Fratesi, R. Gebauer, U. Gerstmann, C. Gougoussis, A. Kokalj, M. Lazzeri, L. Martin-Samos, N. Marzari, F. Mauri, R. Mazzarello, S. Paolini, A. Pasquarello, L. Paulatto, C. Sbraccia, S. Scandolo, G. Sclauzero, A. P. Seitsonen, A. Smogunov, P. Umari, and R. M. Wentzcovitch, J. Phys. Cond. Matt. **21**, 395502 (2009).
[46] J. P. Perdew and A. Zunger, Phys. Rev. B **23**, 5048 (1981).
[47] P. E. Blöchl, Phys. Rev. B **50**, 17953 (1994).
[48] G. Kresse and D. Joubert, Phys. Rev. B **59**, 1758 (1999).
[49] D. Vanderbilt, Phys. Rev. B **41**, 7892 (1990).
[50] Parameters for the ultrasoft pseudopotentials match those of Ref.40. For Pb (not used in Ref.40): $5d^{10}6s^26p^2$, r_0=1.0 bohr, $r_c^{\rm loc}$ = 2.3 bohr, r_c = (2.3,2.5,2.5) bohr for d, s, and p.
[51] H. J. Monkhorst and J. D. Pack, Phys. Rev. B **13**, 5188 (1976).
[52] A. Savin, R. Nesper, S. Wengert, and T. F. Fssler, Angewandte Chemie International Edition in English **36**, 1808 (1997).
[53] R. Seshadri and N. A. Hill, Chem. Mater. **13**, 2892 (2001).
[54] U. V. Waghmare, N. A. Spaldin, H. C. Kandpal, and R. Seshadri, Phys. Rev. B **67**, 125111 (2003).
[55] A. Walsh and G. W. Watson, J. Phys. Chem. B **109**, 18868 (2005).
[56] A. Walsh and G. W. Watson, J. Solid State Chem. **178**, 1422 (2005).
[57] K. Momma and F. Izumi, J. Appl. Crystallogr. **41**, 653 (2008).
[58] G. Sághi-Szabó, R. E. Cohen, and H. Krakauer, Phys. Rev. Lett. **80**, 4321 (1998).
[59] C. H. Peng, J.-F. Chang, and S. B. Desu, in *Symposium G Wide Band-Gap Semiconductors*, MRS Proceedings, Vol. 243 (1991).
[60] R. Gillespie and R. Nyholm, Q. Rev. Chem. Soc. **11**, 339 (1957).
[61] L. Orgel, J. Chem. Soc. **4**, 3815 (1959).
[62] S. M. Nakhmanson and I. Naumov, Phys. Rev. Lett. **104**, 097601 (2010).
[63] P. S. Halasyamani, Chem. Mater. **16**, 3586 (2004).